



Healy, F. J., Cheung, R. C. M., Rezgui, D., Cooper, J. E., Wilson, T., & Castrichini, A. (2024). Experimental and Numerical Nonlinear Stability Analysis of Wings Incorporating Flared Folding Wingtips. *Journal of Aircraft*, 61(1), 140-154. <https://doi.org/10.2514/1.C037167>

Peer reviewed version

License (if available):
CC BY

Link to published version (if available):
[10.2514/1.C037167](https://doi.org/10.2514/1.C037167)

[Link to publication record in Explore Bristol Research](#)
PDF-document

This is the accepted author manuscript (AAM) of the article which has been made Open Access under the University of Bristol's Scholarly Works Policy. The final published version (Version of Record) can be found on the publisher's website. The copyright of any third-party content, such as images, remains with the copyright holder.

University of Bristol - Explore Bristol Research

General rights

This document is made available in accordance with publisher policies. Please cite only the published version using the reference above. Full terms of use are available:
<http://www.bristol.ac.uk/red/research-policy/pure/user-guides/ebr-terms/>

Experimental and Numerical Nonlinear Stability Analysis of Wings Incorporating Flared Folding Wingtips

Fintan Healy^{*}, Ronald Cheung[†], Djamel Rezgui[‡] and Jonathan Cooper[§]
University of Bristol, Bristol, BS8 1TR, UK

Thomas Wilson[¶] and Andrea Castrichini^{||}
Airbus Operations Ltd, Bristol, BS34 7QQ, UK

Recent studies have considered the use of wings incorporating flared folding wingtips (FFWTs) to enable higher aspect ratios - reducing overall induced drag - whilst also reducing gust loading and meeting airport operational requirements. This paper presents the first experimental research into the nonlinear dynamic behaviour of a wing incorporating an FFWT. Wind tunnel tests were conducted at a range of velocities below and beyond the linear flutter boundary. The experimental findings are compared with results obtained from continuation and bifurcation analyses on a representative low fidelity numerical model. The results show that beyond the linear flutter boundary stable Limit Cycle Oscillations (LCOs) form, which dependent on the flare angle, are bounded by either geometric or aerodynamic nonlinearities. Also presented is the effect of a wingtip trim tab on the stability boundary of a wing incorporating FFWTs. It is found that the tab angle can significantly alter the stability boundary of the system, indicating both that the choice of camber is an important parameter when considering the stability boundary of FFWTs, and that a moveable control surface on an FFWT could be used ‘in-flight’ to extend the stability boundary of an aircraft.

Nomenclature

Symbols

α	= angle of attack
β	= wingtip tab angle
η	= twist of the flexural axis
Γ	= dihedral angle
Λ	= flare angle
ρ	= material density; air density
$\mathbf{R}_n(m)$	= rotation matrix about n^{th} axis by m radians
θ	= fold angle
\mathbf{q}	= generalised coordinates
a	= lift curve slope
b	= wing semi-span
c	= chord
C_d	= drag coefficient
C_l	= lift coefficient

C_N	= normal force coefficient
EI	= flexural rigidity
GJ	= torsional rigidity
k	= reduced frequency
M	= number of bending shape functions
N	= number of torsional shape functions
T	= kinetic energy
t	= time
U	= strain energy
w	= vertical velocity component
z	= vertical deformation of the flexural

Subscripts

g	= due to the geometry
h	= property at the tip of the inner wing
i	= property in local frame

Presented as paper 2022-0657 at the AIAA Scitech 2022 Forum, January 3-7, 2022

^{*}PhD Student, Department of Aerospace Engineering. fintan.healy@bristol.ac.uk

[†]Research Associate, Department of Aerospace Engineering.

[‡]Senior Lecturer, Department of Aerospace Engineering.

[§]Airbus RAEng Sir George White Professor of Aerospace Engineering, Department of Aerospace Engineering, FAIAA

[¶]Loads and Aeroelastics Expert

^{||}Loads and Aeroelastics Engineer, Flight Physics

p = property of the 3D printed beam t = property of the wingtip
 s = property of the steel beam

I. Introduction

In 2018, the aviation industry accounted for approximately 3.5% of all anthropogenic radiative forcing [1]. Recent initiatives such as the ICAO *CORSIA* scheme aim to place a cost on emissions [2], incentivizing the aviation industry to develop more efficient aircraft. Next-generation designs such as the truss-based wing and double-bubble concepts [3, 4] aim to achieve this goal by significantly increasing the aspect ratio, and therefore wingspan of the aircraft. This increase in aspect ratio can significantly reduce the lift-induced drag, which at cruise can account for approximately 40% of the total drag of an aircraft [5]. However, increasing the wingspan also affects ground operations, with current infrastructure at many airports - such as gate, runway and taxiway separation - only capable of servicing aircraft up to a specific wingspan [3, 6].

Military aircraft have been mitigating these issues on aircraft carriers since as early as the first world war by using folding wingtip (FWT) devices [7]- in which the span of the aircraft can be shortened by folding the wingtip's up on the ground. More recently this concept has been used in civil applications, with the most notable example being the Boeing 777X [8]. The use of FWTs allows the 777X to fit into the same 65m gate as its predecessor, whilst also being able to increase its wingspan by 7 metres in flight.

In the wider field of morphing aircraft, changing the geometry of a wing in flight can enhance the overall efficiency or performance of an aircraft [9]. However there is typically a trade-off between the cost and complexity of including such a mechanism, and its associated benefits. In the case of the 777X, whilst the wingtips can only be operated on the ground, the inclusion of such a mechanism has already been justified. This raises the question as to whether such a device could be utilised in-flight for additional aerodynamic or structural benefits.

Research into wingtip morphing devices can generally be split into three design motivations: control authority [10–12], increasing aircraft performance across different flight phases [13–16], and load alleviation [17–21]. In the 1960s, test flights of the XB-70 Valkyrie supersonic research aircraft utilised folding wingtips to improve the aircrafts' lift-to-drag ratio. The XB-70 could fold its wingtips down during supersonic cruise, reducing trim drag by moving the centre of pressure forward and increased compression lift by 'capturing' the shock waves from the engine inlet [13].

At transonic speeds, multiple studies [14–16] have shown numerically that improvements to the lift-to-drag ratio of an aircraft can be achieved by varying the 'cant' angle* of a wingtip during different flight phases. Similarly, albeit not inherently an FWT, Eguea et al. [22] proposed a winglet with active camber control to improve the efficiency of an typical business jet across multiple flight phases, with a 6% saving in bulk fuel consumption achieved.

Regarding control authority, Bourdin et al. [10, 11] proposed using a pair of winglets with an adjustable cant angle on a baseline flying wing. Numerical and experimental results showed that by utilising the rearwards centre of pressure of the wingtip relative to the body, pitch and roll control could be achieved by varying the cant angle of both winglets either symmetrically or asymmetrically. More recently, Mills and Ajaj [12] have shown experimentally that the same concept is feasible on a straight wing, however, they also highlighted that roll-control-reversal occurs at negative angles of attack.

Regarding load alleviation, one concept that has gathered traction over the last few years is that of the flared folding wingtip (FFWT) [17–21, 23–25]. As illustrated in Fig. 1, this device consists of a FWT in which the hinge line is rotated to move the intersection with the leading edge outboard so that the hinge line is no longer parallel with the oncoming flow. The magnitude of this rotation is defined as the flare angle, Λ . In this configuration an increase in the fold angle, θ , produces a decrease in the local angle of attack (AoA), and vice versa in the other direction. Therefore, when an FFWT is free to rotate, the fold angle tends to an equilibrium position, defined as the coast angle, about which the aerodynamic and gravitational moments about the hinge balance, and system is statically stable.

Experimental and numerical research has focused on the use of FFWTs as a passive gust and manoeuvre load alleviation device [17–19, 21, 23, 24], as the large spanwise moment arm of a wingtip means it has a significant impact on the bending stresses seen along the wingspan. Such a device is not actually new; with similar devices being used: on the Rey R.1 aircraft, which first flew in 1949, for gust load alleviation [26], and in the 'floating wingtip fuel tank' which was tested to extend the range of both helicopters [27] and fixed wing aircraft [28] independently. Beyond load alleviation, more recent research has focused on the effect of FFWTs on the handling qualities of an aircraft, with both

*The cant angle is defined as the angle of rotation of the wingtip from the normal position, and can be thought of as a change in the dihedral angle of the wingtip.

numerical and experimental studies indicating that the roll performance of a wing incorporating FFWTs is comparable to that of one without the additional span [20, 23, 25].

Additionally, the inclusion of a hinge with zero stiffness means fold angles greater than 20 degrees can easily be achieved. Such large deformations are analogous to those seen in the modelling of highly flexible wings [29], and can introduce geometric and aerodynamic nonlinearities that significantly affect the overall system behaviour, which cannot be adequately predicted using linear methods. Such nonlinearities have been found to have a significant effect on the behaviour of systems including FFWTs, with the authors in [30] highlighting that when the primary flutter mechanism incorporates the motion of the FFWT, the linear flutter boundary is dependent on the attitude of the aircraft - with wind tunnel experiments demonstrating a 30% change in the linear flutter boundary. This behaviour was found to be linked to the coast angle of the FFWT, raising the question as to whether an aerodynamic device placed on the wingtip itself could affect both the coast angle and the dynamic behaviour of the system.

One other important consideration of aircraft that exhibit large nonlinearities is the emergence of limit cycle oscillations (LCOs), which are a common theme throughout the research in the field of nonlinear aeroelasticity [31]. LCOs are a periodic solution with a finite amplitude and typically bound the growth of linear instabilities. Research into the behaviour of LCOs for a wing incorporating FFWTs is limited, with two numerical studies predicting the emergence of LCOs bounded by either aerodynamic [32] or geometric [33] nonlinearities.

Nonlinear numerical methods are required to study phenomena such as LCOs; numerical integration is commonly used for this purpose, and indeed was the primary methodology used in the aforementioned studies on FFWTs [32, 33]. However, as simulations must be run at multiple flight conditions, it is often expensive to both simulate and track nonlinear behaviours using this technique.

Bifurcation analysis, which typically comprises of both bifurcation theory and numerical continuation, offers an alternative tool to assess the stability of nonlinear aeroelastic systems [34–36]. A bifurcation occurs when a small change in a parameter, such as the wind speed, leads to a sudden qualitative change in the stability of a system, such as occurs with flutter. Whereas, numerical continuation can be used to both track the evolution of equilibrium or periodic solutions as a parameter is varied, as well as detect and track the evolution of bifurcations.

In regards to aeroelasticity, Alighanbari and Price [37] first used these techniques to analysis the effect of structural nonlinearities on a two-dimensional airfoil. Since then, bifurcation analysis has been used to study multiple nonlinear aeroelastic systems and phenomena, such as: panel flutter [38], control surface freeplay [39], the dynamics of highly flexible wings [35] and whirl flutter [36], to name but a few. Overall, the use of bifurcation analysis is highly advantages when compared to numerical integration, as it allows an engineer to rapidly explore the parameter space, revealing the complex stability picture of nonlinear systems in a way that would have been difficult to measure using other techniques.

In this paper a flexible wind tunnel model, and an equivalent low-fidelity nonlinear numerical model utilising bifurcation analysis, were used to explore the nonlinear dynamics of FFWTs before and after the linear flutter boundary.

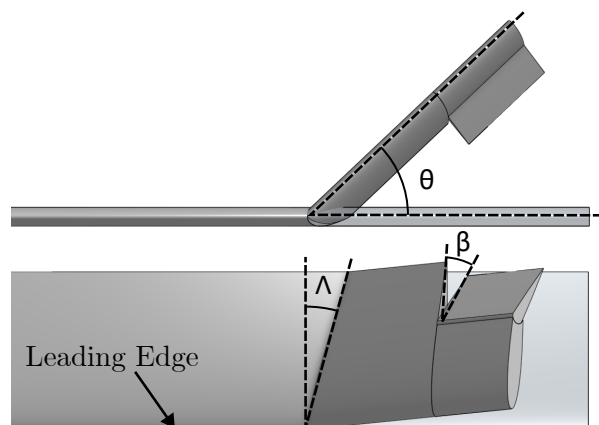


Fig. 1 Representation of a flared folding wingtip device, with a flare angle, Λ , of 15 degrees, at 0 and 45 degrees fold angle, θ , and a wingtip tab deflection, β , of 45 degrees

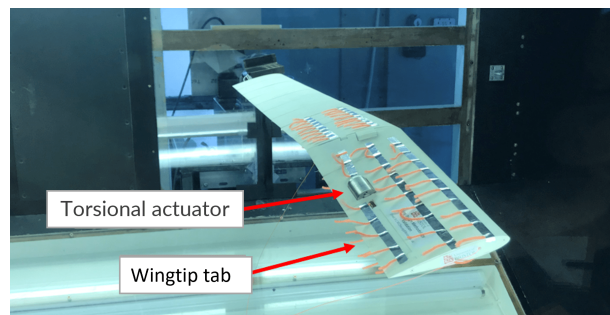


Fig. 2 The wind tunnel model pictured at a stable equilibrium position

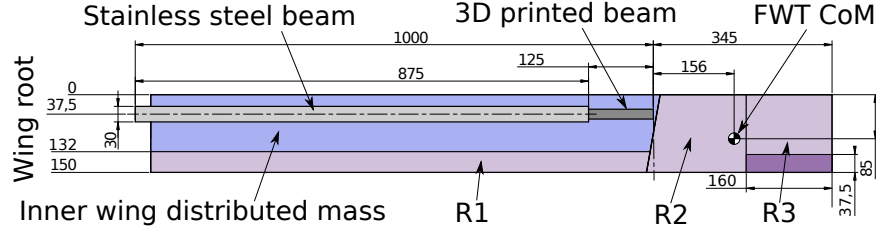


Fig. 3 A schematic of the internal structure of the experimental wing, as modelled in the numerical model.



Fig. 4 An overview of the flexible semi-span model Instrumentation

Additionally, this paper explores how the wings stability boundary is affected when using a movable secondary aerodynamic surface on the trailing edge of the FFWT.

II. Description of Experimental Setup

A. Model Design

This work considers a series of tests conducted using a highly flexible semi-span model which has been used in previous studies [21, 40]. The model, which is shown in Fig. 2, is a straight symmetric wing with a semi-span of $1.345m$, a constant chord length of $15cm$, and a constant cross-sectional NACA0015 profile. The wing is split into two sections by a hinge, and the hinge line intersects the semi-chord line at a span of one metre. By replacing a steel plate across the hinge the model could be tested in either a hinge-free or hinge-locked configuration.

Additionally, as shown in Figs. 1 and 2, a movable secondary aerodynamic surface, referred to as the wingtip tab, is featured on the folding wingtip at the 75% chord position. The wingtip tab has a span of $10cm$ and is driven directly by a Maxon EC-i30 brushless motor[†]. The angle of the wingtip tab, with respect to the chord line of the wingtip is denoted β , as shown in Fig. 1

As shown in Fig. 3, the construction of the inner wing consisted of a stainless steel beam spanning the majority of the inner span, with a 3D printed beam making up the final section of the inner wing. This 3D printed beam directly formed the structure of the hinge, allowing multiple flare angles to be built and then replaced on the model easily. Both beams ran along the quarter chord line, had a rectangular cross-section and had the properties shown in Table 1. As shown in Fig. 4, nine aerodynamic panels slid on to the inner beam. Each of these panels were separated by a small gap, therefore the majority of the wings structural stiffness came from the beams alone.

The inertial properties of the experimental model are shown in Table 2. The first eight inner panels had a mass of $142g^{\ddagger}$. The centre of the first panel had a spanwise position of $85mm$ and there was spacing of $110mm$ between the centre of each of the first eight panels. The ninth aerodynamic panel (denoted the ‘hinge panel’ in Table 2) was both longer and included the hinge assembly, leading to the larger mass in Table 2. The total mass and estimated moment of inertia of the wingtip assembly are also included in Table 2.

As illustrated in Fig. 4, the model was equipped with an RLS RM08 magnetic encoder[§] in the hinge, a Wheatstone bridge measuring the bending moment at the root, and 6 accelerometers distributed across the wing. All sensors were

[†]Maxon Motor Ltd. url:https://www.maxongroup.co.uk/ [retrieved 26 April 2022]

[‡]which includes $40g$ to account for the average mass of bolts and cables within the wing structure

[§]RLS, RM08 Miniature Rotary Magnetic Encoder, url:https://www.rls.si/eng/rm08-super-small-non-contact-rotary-encoder [retrieved 26 April 2022]

Table 1 Properties for the rectangular beams within the inner wing section

Section	Steel Beam	3D Printed Beam
Material	316L Stainless Steel	Polyamide
Cross-section	Rectangular	Rectangular
Width [mm]	30.0	19.3
Height [mm]	5.0	13.3
Density [kgm^{-3}]	8000	3304
Youngs Modulus (E) [GPa]	193	1.65
Poisson's Ratio	0.27	0.3

Table 2 Inertial properties of the experimental model

Item	Mass [g]	x_c [mm]	y_c [mm]	I_{xx} [kg mm^2]	I_{yy} [kg mm^2]
Inner Wing Panels	142	27.5	$85 + 110i$	84.6	171.3
Hinge Panel	247	37.5	952	355.3	221.6
Wingtip	563	47.5	1156	6700.0	615.0

connected to a National Instruments PXIe-6363[¶] card hosted in a National Instruments PXIe-1082 chassis, with the Matlab Data Acquisition API [41] being utilised to both collect the data and control the wingtip tab angle.

B. Model Characterisation

To assess the experimental models natural frequencies and modes shapes, a series of impact hammer tests were performed on the experimental model in the wingtip ‘locked’ configuration. Only the response of the tri-axis accelerometer located just inboard of the hinge (see Fig. 4) was recorded during each impact, with the impact force being applied at 16 locations evenly space along the leading and trailing edge of the model. To capture the out-of-plane and torsional modes the impact force was applied vertically, where as to capture the in-plane modes the impact force was also applied horizontally.

Each impact at each location was repeated three times and the average frequency response function (FRF) at each location was used to extract the natural frequencies and corresponding modeshapes of the wing via a least-squares rational function estimation method [42]. The identified natural frequencies below 50 Hz are reported in Table 3, along with the corresponding mode shapes of the structure.

Additional modal characterisations at a flight velocity of 18 m s^{-1} are presented by Cheung et al. [40], who utilised a random gust excitation to measure the modal frequencies of the same experimental model. The numerical model developed in the next section is compared to these results in section IV.

Table 3 The first 6 natural frequencies and corresponding modeshapes of the experimental model

Modeshape	Frequency [Hz]
Out-of-plane 1	1.65
Out-of-plane 2	8.78
In-plane 1	9.07
Out-of-plane 3	22.44
Torsion 1	30.51
In-plane 2	30.74

[¶]National Instruments, PXI Systems, URL:<https://www.ni.com/en-gb/shop/pxi.html> [retrieved 26 April 2022]

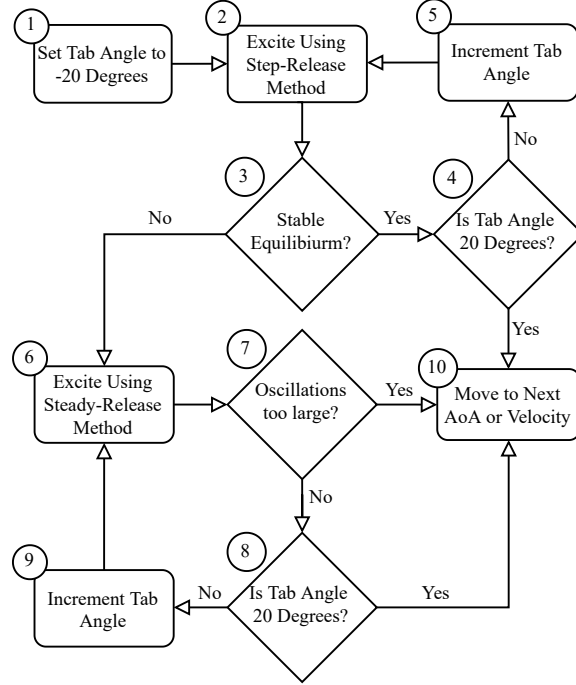


Fig. 5 The procedure used during wind tunnel testing at each AoA and velocity.

C. Experimental Methodology

The testing was conducted in the 7ft by 5ft low-speed closed-return wind tunnel at the University of Bristol. The model was tested across: a range of wind speeds between 18 and 33ms⁻¹; a range of AoA between -2.5 and 8.8 degrees; and a range of wingtip tab angles between -20 and 20 degrees.

A cord attached just inboard of the hinge was used to control the model in one of two ways. During a *step-release* test, the model was excited by pulling the cord taut and then quickly releasing it, producing a step response. During a *steady-release* test, the model was stabilised by pulling the cord taut. The cord was then slowly released, allowing any instabilities to grow naturally with time.

The procedure used to test the model at each AoA and velocity is summarised in Fig. 5. At each flight condition, and starting at a tab angle of -20 degrees, the model was first excited using the step release method. If the wingtip returned to a stable equilibrium position the tab angle was incremented and the process repeated. However, if an LCO formed the model was instead excited using the steady-release method, with the tab angle then being incrementally increased until either the magnitude of oscillation was too large or a tab angle of 20 degrees was reached.

III. Numerical Modelling

To complement the experimental data a low-fidelity numerical model was developed to explore the post linear-flutter-boundary behaviour of a wing incorporating an FFWT. The addition of a flexible straight inner wing adds a few key kinematics to an FFWT; a plunging motion, due to the vertical deformation of the tip of the inner wing; a change in the effective AoA due to twist of the inner wing; and a change in the orientation of the zero fold angle, due to a change in the effective dihedral angle at the junction between the inner wing and the wingtip. Therefore, the model described in this section was chosen to be the minimum representation required to capture these effects.

As described in the following sections, the equations of motion were derived using the Euler-Lagrange method. Equations describing the kinetic and potential energy of the structural model are described in section III.A, with the generalised external force due to aerodynamic loads being derived in section III.B.

Two key simplifications were made when developing the numerical model. Firstly, the in-plane modes were not considered, and secondly the flare angle of the FFWT was assumed to be zero in the structural model. These simplifications ensured finding an analytical version of the equations of motion (EoM) was tractable with the chosen methodology, which enabled the rapid exploration of the parameter space. Clearly these simplifications will alter the

dynamic behaviour, however as is shown in the results section, the developed numerical model adequately captures the primary nonlinear effects driving the behaviour of an FFWT.

A. Structural Model

The deformation of the inner wing was modelled using the Rayleigh Ritz assumed shapes method [43, p. 52], with the vertical deformation of the flexural axis (z) and its rotation (η) defined respectively as

$$z(y, t) = \begin{cases} \sum_{i=1}^N y^{i+1} q_i(t) & y \leq b_i \\ \left(\sum_{i=1}^N y^{i+1} q_i(t) \right) + (y - b_i)^2 q_{(N+M+1)}(t) & b_i \leq y \leq b_h \end{cases} \quad (1)$$

$$\eta(y, t) = \begin{cases} \sum_{i=1}^M y^i q_{(N+i)}(t) & y \leq b_i \\ \left(\sum_{i=1}^M y^i q_{(N+i)}(t) \right) + (y - b_i) q_{(N+M+2)}(t) & b_i \leq y \leq b_h \end{cases} \quad (2)$$

where α is the AoA of the model, q_i is the i th generalised coordinate, b_h and b_i are the semi-span of the inner wing (or hinge) and stainless steel beam respectively, and N and M are the number of bending and torsional shape functions respectively (which for the purposes of this model were chosen as $N = 3$ and $M = 2$). The piecewise nature of Eqs. (1) and (2) is due to the two sections of beam which make up the inner wing, where one additional shape function was added in both bending and twist, beyond a semi-span of b_i , to account for the significant difference in stiffness between the steel and 3D printed beam sections. Likewise, the beam strain energy was modelled in a piecewise fashion using Euler-Bernoulli beam theory, such that

$$U = \frac{1}{2} \left(\int_0^{b_i} E_s I_s \left(\frac{\partial^2 z}{\partial y^2} \right)^2 dy + \int_{b_i}^{b_h} E_p I_p \left(\frac{\partial^2 z}{\partial y^2} \right)^2 dy + \int_0^{b_i} G_s J_s \left(\frac{\partial \eta}{\partial y} \right)^2 dy + \int_{b_i}^{b_h} G_p J_p \left(\frac{\partial \eta}{\partial y} \right)^2 dy \right) \quad (3)$$

where EI and GJ are the flexural rigidity and the torsional rigidity of the inner wing respectively, and the subscripts s and p represent the properties of the steel beam and 3D printed beam respectively.

Each beam section has a uniform mass distribution, and the secondary mass of the inner wing was modelled through an additional uniform mass distribution, as shown in Fig. 3. This secondary mass distribution had a total mass of 1.38 kg, denoted m_w , and spanned from the leading edge to a chordwise position of 13.6 cm, denoted c_w , ensuring the inner wing had a similar mass distribution to that of the experimental model. Therefore, the kinetic energy of the inner wing could be calculated as

$$T = \frac{1}{2} \left(\int_0^{b_i} \int_{-\frac{1}{2}w_s}^{\frac{1}{2}w_s} \rho_s d_s \dot{z}^2 dx dy + \int_{b_i}^{b_h} \int_{-\frac{1}{2}w_p}^{\frac{1}{2}w_p} \rho_p d_p \dot{z}^2 dx dy + \int_0^{b_h} \int_{-x_f}^{c_w - x_f} \frac{m_w}{c_w b} \dot{z}^2 dx dy \right) \quad (4)$$

where w , d and ρ are the beam width, depth and density respectively, and x_f is the distance between the leading edge and the flexural axis, which was located along the quarter chord line.

The wingtip was modelled as a rigid point mass connected to the tip of the inner wing via a hinge. As this paper predominantly focuses on a small flare angle of 10 degrees, to significantly simplify the equations of motion, it was assumed that the hinge had a flare angle of zero degrees in the structural model. Therefore, the position of the wingtip point mass in the global coordinate system was denoted

$$\vec{p}_{\text{fwt}} = \begin{bmatrix} 0 \\ b_h \\ z(b_h, t) \end{bmatrix} + \mathbf{R}_y(\eta(b_h, t)) \mathbf{R}_x(\theta) \begin{bmatrix} x_t \\ y_t \cos \theta \\ y_t \sin \theta \end{bmatrix} \quad (5)$$

where x_t , y_t represents the displacement of the wingtips CoM from the flexural axis of the hinge, θ represents the fold angle, and the operator $\mathbf{R}_n(m)$ defines a 3D rotation matrix, which describes an anti-clockwise rotation about the n^{th} axis by m radians. The potential energy of the wingtip was defined as

$$U_t = -m_t (\mathbf{R}_y(\alpha) \mathbf{p}_{\text{fwt}} \cdot \mathbf{g}) \quad (6)$$

where m_t is the mass of the wingtip, \mathbf{g} is the acceleration due to gravity and $\mathbf{R}_y(\alpha)$ is an additional rotation to account for the models AoA. The kinetic energy of the wingtip was calculated using the concept of the *Body Jacobian Matrix* [44, p. 117], \mathbf{J}_b , such that

$$T_t = \mathbf{J}_b^T \mathbf{M}_t \mathbf{J}_b \quad (7)$$

where \mathbf{M}_t is the generalised inertia matrix of the wingtip. It is a square, diagonal, matrix and its trace is equal to

$$\text{Trace}(\mathbf{M}_t) = [m_t, m_t, m_t, I_{xx}, I_{yy}, I_{zz}] \quad (8)$$

where I_{xx} , I_{yy} and I_{zz} are the moments of inertia of the wingtip about the centre of mass. The inertial properties used for the wingtip in the numerical model are the same as those shown in Table 2. Using the derived equations for the kinetic and potential energy of each element, the equations of motion of the entire system were found using the Euler-Lagrange method, utilising the python package sympy [45], and were of the form

$$\mathbf{M}(\mathbf{q}, \dot{\mathbf{q}}) \ddot{\mathbf{q}} - \mathbf{f}(\mathbf{q}, \dot{\mathbf{q}}) = 0 \quad (9)$$

where \mathbf{M} is the mass matrix, \mathbf{f} is a matrix of additional forces, and \mathbf{q} is the state vector of the system. In total the system has eight states: three bending and two torsional shapes for the inner wing; one additional bending, and one additional torsional shape for the 3D printed beam; and one rotational degree of freedom about the hinge.

It is important to note that Eq. (5) - which describes the rotation of the wingtip about the hinge - provides the only source of geometric nonlinearity within the structural model. The resulting nonlinear variations in the wingtips potential energy lead to changes in the generalised gravitational forces applied to the model via the vector \mathbf{f} , and the variations in kinetic energy will alter both the generalised mass matrix, \mathbf{M} , as well as the generalised inertial forces applied via the vector \mathbf{f} .

B. Aerodynamic Model

The aerodynamic forces acting on the wing were modelled using modified unsteady strip theory at a discrete number of strips. The wing was split into three discrete regions (R1, R2 and R3 in Fig. 3). The first region spans the entire inner wing as was split into 20 uniform strips. The second region extends from the hinge to the start of the wingtip tab, and the third region extends to the tip of the wing. Both the second and third region were split into 10 uniform strips. At each strip the local AoA was calculated as

$$\alpha_i(\mathbf{q}, \dot{\mathbf{q}}, y) = \alpha_g + \arctan\left(\frac{w(\mathbf{q}, \dot{\mathbf{q}}, y)}{V}\right) \quad (10)$$

where α_g represents the local geometric AoA and w represents the local vertical velocity due to the motion of the wing. For the inner wing $\alpha_g = \eta(y, t)$. For the FFWT the local geometric AoA is approximated as α_f , which is defined using a geometrically exact representation of the local AoA as presented by Healy et al. [30]. This formulations uses a set of rotation matrices to calculate the local velocity vector in a reference frame centred about the FFWT, such that

$$\mathbf{v}_f = \begin{bmatrix} v_{f0} \\ v_{f1} \\ v_{f2} \end{bmatrix} = \mathbf{R}_z(-\Lambda) \mathbf{R}_x(\theta) \mathbf{R}_z(\Lambda) \mathbf{R}_x(\Gamma_h) \mathbf{R}_y(\alpha_r + \alpha_h) \begin{bmatrix} \|\mathbf{V}\| \\ 0 \\ 0 \end{bmatrix} \quad (11)$$

$$\alpha_f = \arctan \frac{v_{f2}}{v_{f0}} \quad (12)$$

where V is the wind speed velocity, α_r is the root AoA, and α_h and Γ_h are the local AoA and dihedral angle at the tip of the inner wing respectively, and are defined as

$$\alpha_h = \eta(b_h, t) \quad (13)$$

$$\Gamma_h = \frac{\partial z(b_h, t)}{\partial y} \quad (14)$$

To account for 3D effects, the local lift-curve-slope at each panel, a_i , was interpolated from a set of lift distributions that were pre-calculated using lifting line theory and the python package *Aerosandbox* [46]. The purpose of this paper was not to accurately predict the lift distribution, as it is likely to vary as a function of not only velocity and root AoA

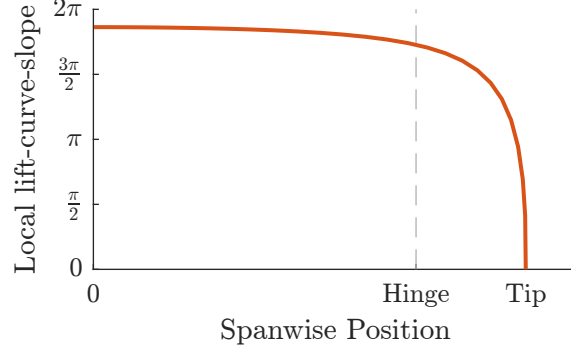


Fig. 6 The spanwise variation in the local lift-curve slope used on the numerical model.

but also the wingtips fold angle . Therefore, a lift distribution was calculated to best represent the mean case at a root AoA of 5 degrees and a fold angle of zero degrees, with an example variation in the spanwise lift-curve-slope shown in Fig. 6. In terms of an FFWT, it is the force normal to the surface that contributes to the moment balance about the hinge[‡], such that

$$F_{N_i} = \frac{1}{2} \rho V^2 c C_{N_i} \quad (15)$$

$$C_{n_i} = C_{l_i} \cos \alpha_i + C_{d_i} \sin \alpha_i \quad (16)$$

where F_{n_i} is the local force normal to the aerofoil surface, C_{d_i} is the local drag coefficient and C_{n_i} is the local normal force coefficient. As shown in Fig. 7, this was accounted for by modifying the lift-curve slope to have the same mean gradient as the normal force coefficient calculated across a weighted average of viscous *XFOIL* [47] predictions (across the experimental range of Reynolds numbers). Additionally, a basic stall correction was applied to the normal force coefficient of the form

$$C_{n_i} = a_i \left(\frac{1}{\sigma} \ln \left(\frac{1 + e^{\sigma(\alpha_i + \alpha_s)}}{1 + e^{\sigma(\alpha_i - \alpha_s)}} \right) - \alpha_s \right) \quad (17)$$

Equation (17) is an adaptation of the ‘soft clipping activation function’ [48], in which σ is a factor that defines the sharpness of the transition from the attached to stalled regime, and α_s is the local AoA at which the model stalls. This formulation, which is illustrated in Fig. 7, was chosen because it is both continuous and its derivative is effectively constant for a significant proportion of the attached regime. Throughout this paper the values of σ and α_s were chosen as 80 and 13 degrees respectively, to give the best compromise between maximum C_n and matching the point of stall, as shown in Fig. 7.

To model the effect of the wingtip tab, a correction was applied to the normal force and moment coefficient’s of the strips in region three of Fig. 3. These correction were of the form

$$C_{n\beta} = C_{n_i} + a_i C_{n\beta} \beta \quad (18)$$

$$C_{m\beta} = a_i C_{m\beta} \beta \quad (19)$$

where the coefficients $C_{n\beta}$ and $C_{m\beta}$ equalled 0.302 and -0.045 respectively and where estimated by interpolating a series of 2D *XFOIL* [47] simulations.

Finally, a process similar to that used by Delaurier [49], was used here to model the influence of unsteady aerodynamic vortex-wake effects. α_i was replaced in Eq. (17) with α'_i , such that

$$\alpha'_i = \frac{AR}{2 + AR} C'(k) \alpha_i \quad (20)$$

where k is the reduced frequency, AR is the aspect ratio, and $C'(k)$ is an approximation of the Theodorsen function for a elliptical wing executing simple harmonic motion, first derived by Scherer [50], such that

$$C'(k) = F'(k) \alpha + \frac{c}{2V} \frac{G'(k)}{k} \dot{\alpha} \quad (21)$$

[‡] as the aerofoil section of the experimental model is symmetric the effect of pitching moment has been neglected in this analysis

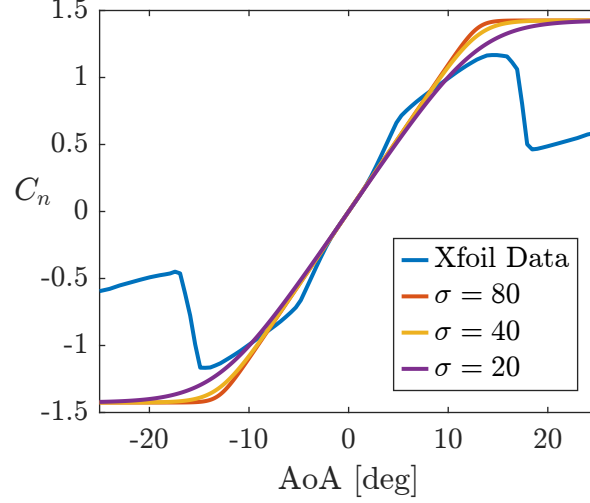


Fig. 7 A comparison between XFOIL viscous data for a NACA0015 profile and the 'soft clipping activation function', as described by Eq. (17), for different values of σ

$$F'(k) = 1 - \frac{c_1 k^2}{K^2 + c_2^2} \quad (22)$$

$$G'(k) = -\frac{c_1 c_2 k^2}{K^2 + c_2^2} \quad (23)$$

$$c_1 = \frac{AR}{2(2.32 + AR)} \quad (24)$$

$$c_2 = 0.181 + \frac{0.772}{AR} \quad (25)$$

Aerodynamic forces were converted into generalised coordinates using the principle of equal wrench's [44], which emanates from D'Alembert's principle. Leading to the final form of the equations of motion as

$$\mathbf{M}(\mathbf{q}, \dot{\mathbf{q}}) \ddot{\mathbf{q}} - \mathbf{f}(\mathbf{q}, \dot{\mathbf{q}}) = \mathbf{e}(\mathbf{q}, \dot{\mathbf{q}}) \quad (26)$$

where $\mathbf{e}(\mathbf{q}, \dot{\mathbf{q}})$ represents a vector of external forces, including aerodynamic forces.

C. Stability Analysis Methods

As well as the use of time simulations to qualitatively verify the stability of a system, numerical continuation and bifurcation theory were used to assess the stability of nonlinear aeroelastic systems [34–36]. These methods have been widely used for investigating the nonlinear dynamics of many aeroelastic and aeromechanic systems and they have shown their usefulness in revealing the complex stability picture of these nonlinear systems. Starting at a known solution, numerical continuation calculates the variation in the steady state solution when a 'continuation parameter' is altered [51], drawing an arc in phase space - denoted a 'branch'. At points at which the stability of the system qualitatively changes (such as at the onset of flutter or divergence in the case of an aeroelastic system) a bifurcation point will occur. This signifies the potential start of a number of other branches dependent on the type of bifurcation. Typically, the computed branches can either be equilibrium positions of the system in phase space, or periodic solutions (otherwise know as LCOs).

The stability of equilibrium branches can be calculated using eigenvalues analysis on a local linearisation of the nonlinear system. Only one mode of the system has to be unstable for an overall system instability, with the stability of each mode determined by the sign of the real component of the corresponding eigenvalue, negative being stable. On the other hand, Floquet theory is used to determine the stability of periodic solutions [52].

For this study the key type of bifurcation is the Hopf bifurcation, at which point the stability of an equilibrium branch changes, and a periodic solution emerges (i.e. an LCO). This bifurcation is caused by a complex conjugate pair of eigenvalues crossing the imaginary axis in the complex plane.

Table 4 Key to symbols and lines used in bifurcation diagrams











Graphic	Description	Meaning
	Solid green Line	Stable equilibrium branch
	Dashed magenta line	Unstable equilibrium branch
	Solid dark blue line	Stable periodic solution branch (max. amplitude of LCO)
	Solid light blue line	Stable periodic solution branch (min. amplitude of LCO)
	Dotted red line	Unstable periodic solution branch (max. or min. value of LCO)
	Grey Solid Line	Locus of Hopf bifurcations calculated using two parameter continuation
	Hollow square	Hopf bifurcation
	Solid green triangle	Experimental data - Stable equilibrium (mean value)
	Solid magenta triangle	Experimental data - Unstable equilibrium (mean value)
	Solid blue square	Experimental data - Stable LCO (max. or min. value)

Table 5 The natural frequencies measured experimental by Cheung et al. [40] in the hinge-free configuration, at a wind speed of 18 m s^{-1} and an AoA of 5 degrees, compared to those measured by the numerical model.

Modeshape	Exp. [Hz]	Num. [Hz]	Delta [%]
Flapping	1.34	1.33	0.8%
Out-of-plane 1	2.29	2.32	1.3%
Out-of-plane 2	14.63	15.49	5.9%
In-plane 1	6.74	-	-
Torsion 1	-	36.2	-

In this paper, bifurcation diagrams - which are a 2D projection of the branches and bifurcation points that arise as one parameter (known as the continuation parameter) is varied - were produced using the "Dynamical Systems Toolbox for MATLAB" [53], which uses an implementation of AUTO-07P [54]. A key to the symbols and line styles used on the bifurcation diagrams within this paper is shown in Table 4.

IV. Results

To provide an initial validation of the numerical model, the estimated modal frequencies of the system at a flight velocity of 18 m s^{-1} and an AoA of 5 degrees were compared to those presented by Cheung et al. [40]. Table 5 shows that there is a good correlation in the frequency of the wingtip flapping mode and first out-of-plane bending mode. As the numerical model only uses three bending shapes the agreement in the second out-of-plane bending mode is worse and the in-plane modes are not captured in the numerical model. However, in the context of the experimental model, these modes are of less importance as the primary flutter mechanism explored in this paper is dominated by the interaction of the wingtip flapping and first out-of plane bending modes.

To further explore the dynamic behaviour of the experimental model, all of the generalised velocities and accelerations are set to zero in Eq. 9, this leaves an algebraic equation, which can be used to find the 'wind-off' equilibrium position of the numerical model. For a wing incorporating an FFWT, the wingtip should point vertical down in this condition. This behaviour is indeed predicted in Fig. 8a, where at a velocity of zero the fold angle is approximately -84 degrees. Note, this is not exactly -90 degrees due to the inner wing bending down under the effect of gravity, resulting in a negative dihedral angle at the tip of the inner wing, which is shown in Fig. 8b to be approximately -6 degrees.

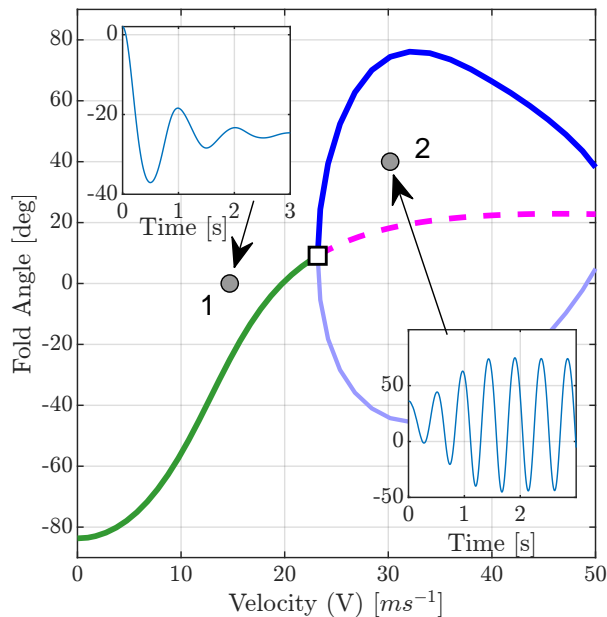
Using numerical continuation, with velocity as the continuation parameter, we can calculate how this equilibrium position varies with velocity. The resulting bifurcation diagram, for a wing at 5.5 degrees AoA, is shown in Fig. 8a. In this figure, the fold angle increases with velocity on a stable equilibrium branch (denoted by the green line) until a velocity of 23.2 m s^{-1} . At which point the stability of the system changes, resulting in a Hopf bifurcation, which is denoted by the white square in Fig. 8a. From this bifurcation three additional branches emerge. The first is an unstable equilibrium branch, and the other two blue lines represent a stable periodic solution.

As mentioned in section III.C, a Hopf bifurcation signifies a complex conjugate pair of eigenvalues crossing the imaginary axis in the complex plane and hence, the corresponding mode becoming unstable. In a purely linear system the oscillations from this unstable oscillatory mode would grow exponentially, however nonlinearities can bound the growth of these oscillations leading to a stable periodic solution. The emergence of this periodic solution is denoted by the blue lines in Fig. 8a, which represent the maximum and minimum fold angles achieved during these periodic oscillations.

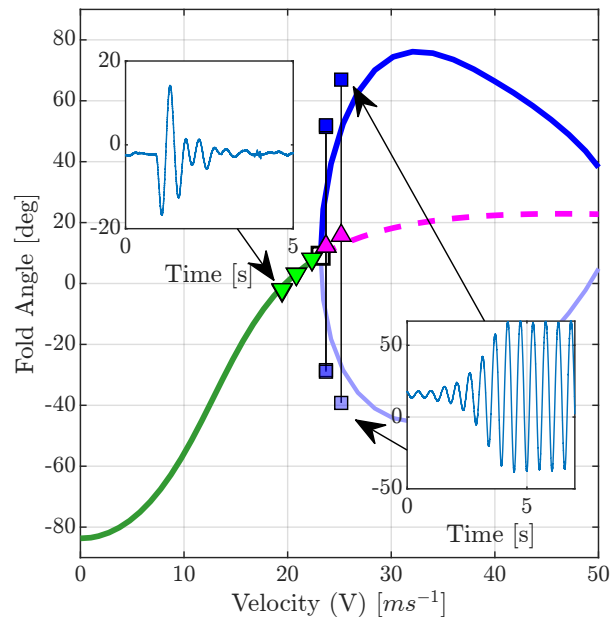
When considering the entire phase space, one can consider the stable branches as attractors and the unstable branches as repellers. In Fig. 8a, if the system starts at point 1, the system will be pulled towards the green equilibrium branch, as shown by the damped oscillatory time response in Fig. 8a. Whereas if the system starts from point 2, it is attracted to the stable periodic solution, with the time response in Fig. 8a showing that an initial perturbation grows until its maximum and minimum amplitude reach those denoted by the blue lines in Fig. 8a.

The mechanism causing the Hopf bifurcation in Fig. 8a can be visualised in a more traditional manner by plotting the variation in the model frequencies and damping ratios about the equilibrium position, with velocity. Such analysis is presented in Fig. 9 and at zero velocity the first mode has a frequency of approximately 1 Hz and corresponds to the pendulum frequency of the wingtip (as the wingtip can swing about the vertical position akin to a pendulum). The second mode has an initial frequency of around 2 Hz, and corresponds to the first out-of-plane bending mode of the inner wing. As the velocity increases so does the rate of change of aerodynamic forces with fold angle. This increases the aerodynamic stiffness of the wingtip mode, increasing its frequency. When these two modes coalesce the damping is significantly reduced in one of the two modes, destabilising the system. Furthermore, due to the frequency separation between the first two modes and the other bending and torsional modes (see Table 5) the dynamics of the numerical model are dominated by the first two modes.

Figure 8b shows a comparison between the numerical and experimental results for the same condition as in Fig. 8a and it can be seen that there is a good correlation between both the stable equilibrium branches and the location of the Hopf bifurcation in both models. In Fig.8b, a black line has been drawn between the experimental unstable equilibrium marker and the two periodic markers at each velocity, this is to highlight to the reader that each experimental periodic solution has a corresponding unstable equilibrium position, and this black line is not repeated in further figures. Additionally, it should be noted that although the magenta triangles in Fig. 8b represent the unstable equilibrium position



(a) Numerical results with example numerical time traces



(b) Experimental and numerical results with example experimental time traces

Fig. 8 Bifurcation diagrams, with example time traces, for the experimental and numerical models at $\alpha = 5.5$ deg, $\beta = 5$ deg, $\Lambda = 10$ deg. In which the dark and light blues lines represent the maximum and minimum value achieved during an LCO

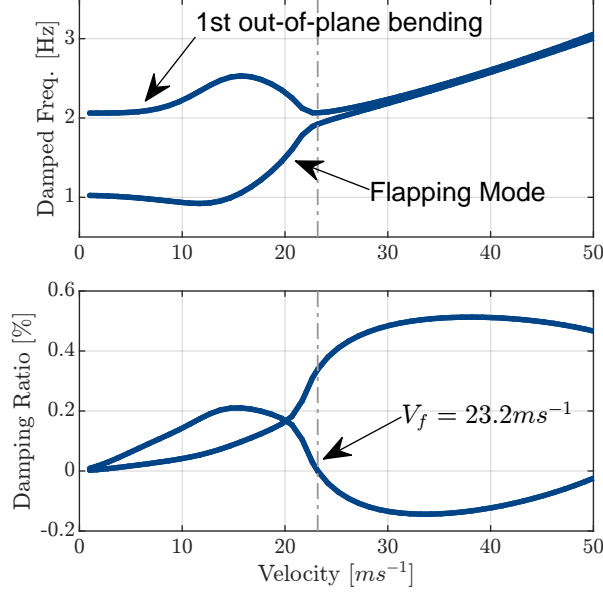


Fig. 9 Variation of damped frequency and damping ratio for the first two modes, with wind speed, at the same conditions shown in Fig. 8b

of the FFWT, this quantity could not be measured directly. Therefore, these markers actually show the mean fold angle across one LCO. Although this means that their location may not be correct, their inclusions allows the experimental bifurcation point to be more easily visualised, which will become important in later figures.

Beyond the linear flutter boundary the amplitude of the stable periodic branch in Fig. 8b grows rapidly, leading to large peak fold angles at around $30 ms^{-1}$ in the numerical model. The rate of growth of the LCO is larger for the experimental data, albeit due to the construction of the hinge in the experimental model, the maximum achievable fold angle was around 70 degrees, limiting the velocities at which the model could be tested. This accelerated growth suggests that either a weaker nonlinearity bounds the motion, or that the velocity of the Hopf bifurcation is slightly smaller in the experimental data. It is also important to note that no periodic solutions were observed below the linear flutter speed in either model, suggesting this is a super-critical Hopf bifurcation [55, p. 170-189]. Therefore, neither model exhibited stable periodic oscillations below the linear flutter speed, regardless of the size of the initial perturbation.

It is important to remember that the fold angle is not the only state of this system. Figure 10 shows four additional projections of this system, namely the wing root bending moment (WRBM), vertical displacement of the hinge, hinge twist angle, and the local AoA at the tip of the wingtip. Firstly, Fig. 10 shows that there is a good correlation between the experimental and numerical WRBMs prior to the Hopf bifurcation**. Beyond the Hopf bifurcation, the LCO shown in Fig. 10 indicates that there is significant movement of the inner wing, with the amplitude of oscillation of the hinge equal to approximately 17% of the inner span, at a velocity of $30 ms^{-1}$. However, Fig. 10 also indicates that the torsional motion of the wing is relatively small during the LCOs and likely does not significantly contribute to the dynamic behaviour of the wing. Additionally, Fig. 10 shows that the local AoA at the tip of the wingtip, which includes the induced AoA due to the motion of the wingtip, rarely goes above the stall angle (13 degrees). Therefore, the LCO in the numerical model is bounded by the geometric nonlinearities due to the large rotations of the wingtip.

Figure 11 shows the same bifurcation diagram as Fig. 8b across a range of AoAs. In general the same trend is seen across all attitudes for both the numerical and experimental models, with an LCO forming beyond a super-critical Hopf bifurcation that grows in amplitude with velocity. Overall Fig. 11 indicates there is a good correlation between the models, indicating that the low-fidelity numerical model captures the primary mechanisms driving both the location of the Hopf bifurcation (i.e. the linear flutter point) and the localised nonlinear behaviour.

Additionally, Fig. 11 and Table 6 indicate that the velocity of the Hopf bifurcation increases with root AoA, and indeed at a root AoA of -5 degrees, the numerical model suggests the wing is stable up to at least $40 ms^{-1}$. By comparing the variation in modal frequencies and damping ratios, Fig. 12 shows that as the AoA is decreased from 5.5

**The WRBM of the numerical model was calculated as $M = EI \frac{d^2z}{dy^2} \Big|_{y=0}$ where z is defined in Eq. (1).

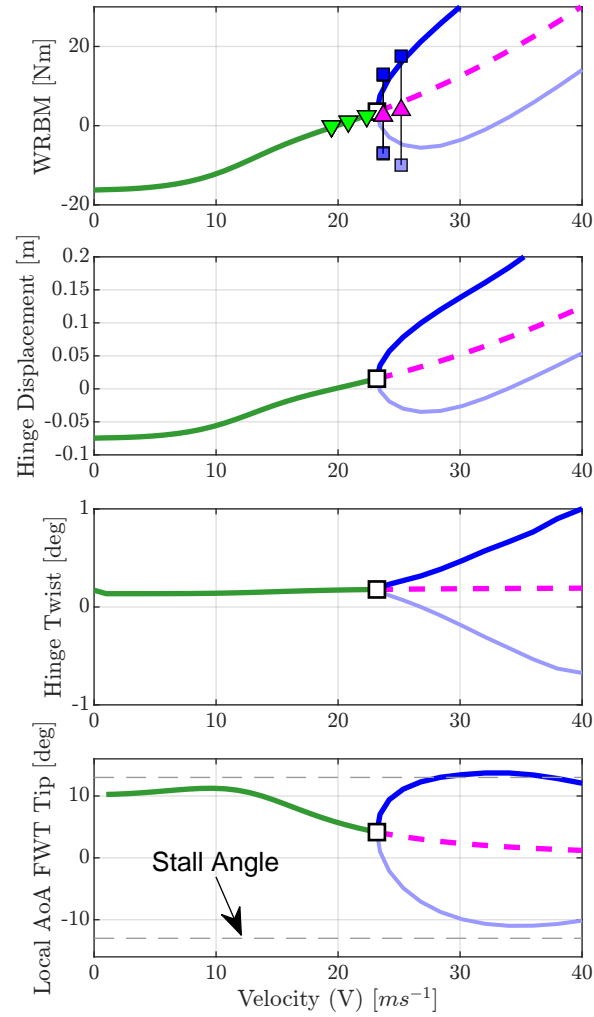


Fig. 10 Three bifurcation diagrams of the numerical model at $\alpha = 5$ deg, $\beta = 0$ deg and $\Lambda = 10$ deg

Table 6 Tabulated flutter speeds for the cases shown in Fig. 11. Experimental values are evaluated as the mean velocity between the last stable and first unstable data point.

AoA [deg]	Experimental [ms^{-1}]	Numerical [ms^{-1}]
-5	-	Stable
-2.5	31.7 ± 0.9	32.0
2.5	26.4 ± 0.8	26.2
5.5	23.0 ± 0.7	23.2
8.8	20.6 ± 0.7	20.7

degrees, the point at which the two mode coalesce varies, changing both the location of the peak negative damping, and its magnitude. At an AoA of -5 degrees the damping ratio does not cross the zero axis and the system remains stable across all velocities presented.

The mechanism for this variation in both the aerodynamic stiffness of the FFWT and the change in the linear flutter boundary with root AoA, are described in detail in [30], in which the authors developed a methodology to linearise an MSC Nastran model of the same wing presented in this paper about different coast angles to predict the linear flutter boundary. As presented in [30], the driving mechanism for the change in aerodynamic stiffness is the rate of change in the geometric AoA of a wingtip with fold angle. Figure 13 shows this relationship, and indicates that the geometric AoA of an FFWT, and its derivative with respect to the fold angle, are a nonlinear function of the fold angle. Furthermore, this derivative can be viewed as a good approximation of the aerodynamic stiffness of the wingtip as it indicates the rate of change of aerodynamic forces with respect to the fold angle.

As the root AoA of a wing is varied, the equilibrium position of the wingtip also varies to ensure the aerodynamic and gravitational moments about the hinge are balanced. This change in the fold angle, alters the aerodynamic stiffness of the wingtip, changing the frequency of the FFWT mode. Therefore, at different root AoAs the velocity at which the first two modes coalesce can vary, altering the linear flutter speed of the model. Figure 13 illustrates that the peak aerodynamic stiffness increases with AoA, and that the variation in aerodynamic stiffness with AoA reduces with increasing flare angle. This effect suggests the minimum flutter speed will occur at higher root AoAs and that there will be more variation in the linear flutter speed at lower flare angles.

Regarding again Fig. 11, we are left with questions such as, "what is the critical root AoA at which the system is always stable?", and "what is the shape of the linear flutter boundary in phase space?". These questions could be answered by running numerical continuation at multiple root AoAs. Alternatively, a more efficient technique is to use two-parameter-continuation [54] to 'track' the location of the Hopf bifurcation in the bifurcation diagram whilst two parameters are varied. In the case of Fig. 14, the grey lines represent the locus of Hopf bifurcations calculated using this technique as both the velocity and the root AoA of the numerical model were varied. This figure indicates that the numerical model is stable below a root AoA of -3.6 degrees and that at higher velocities the model can be re-stabilised.

Experimental tests were also conducted using a hinge with a 30 degree flare angle. Figure 15 compares the experimental and numerical models at a root AoA of -2.5 degrees and flare angles of 10 and 30 degrees, which will be referred to as the *flare10* and *flare30* cases respectively. For the *flare30* case there is a qualitative match between the numerical and experimental models in Fig. 15, with the growth of an LCO by a similar amplitude occurring after a supercritical Hopf bifurcation. There is however approximately a 4 ms^{-1} difference in the predicted velocity of the Hopf

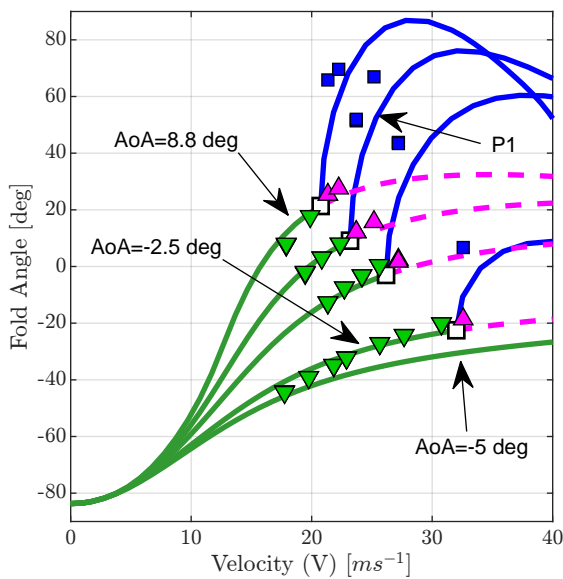


Fig. 11 Bifurcation diagrams of the numerical and experimental model at a flare angle of 10 degrees and 5 AoAs (-5, -2.5, 2.5, 5.5 and 8.8 deg)

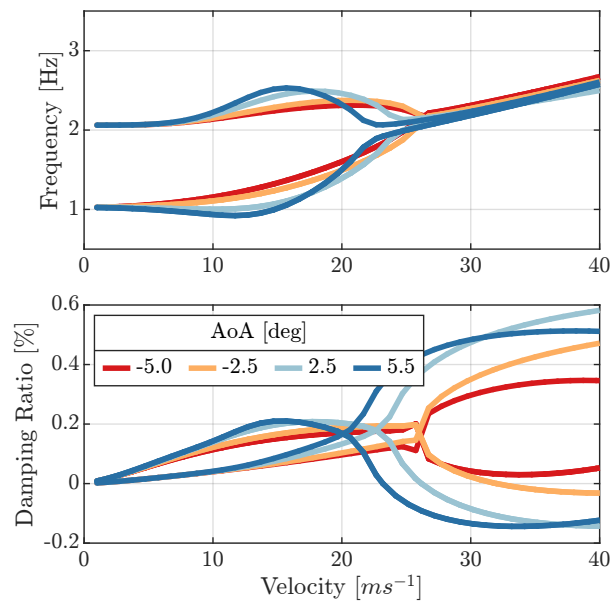


Fig. 12 Variation of damped frequency and damping ratio for the first two modes, with wind speed, for different AoAs

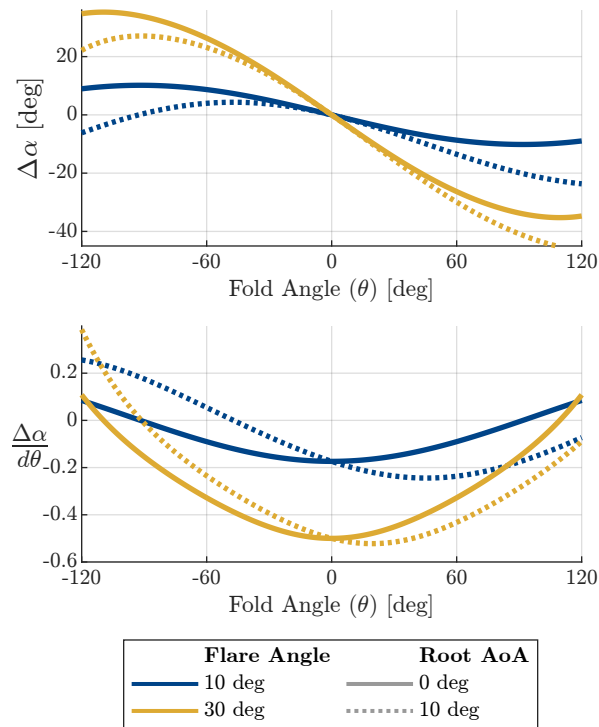


Fig. 13 Variation in the local geometric AoA and its derivative, with fold angle, on a folding wingtip, at multiple flare angles and root AoAs

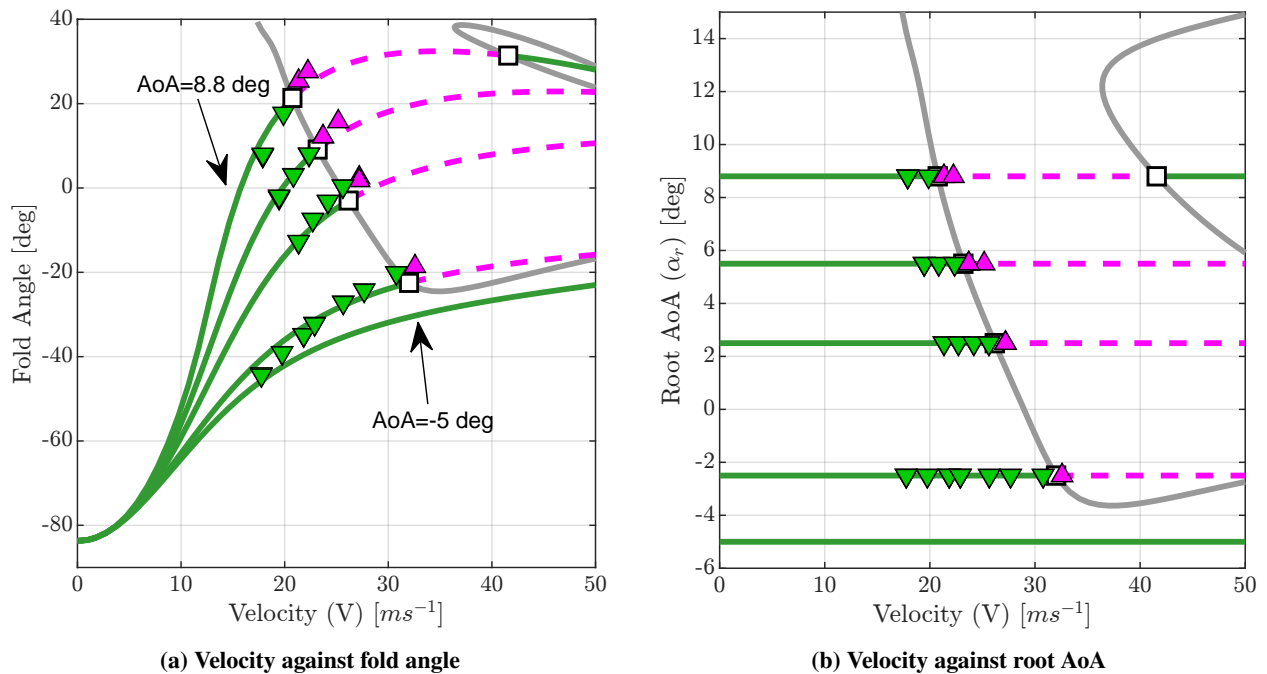


Fig. 14 Bifurcation diagrams in two-parameter space (b) with the corresponding bifurcation diagram in the fold angle projection (a), at a flare angle of 10 degrees

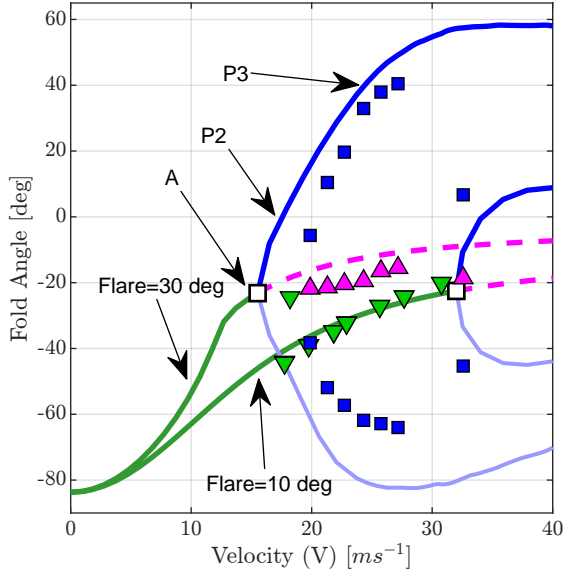


Fig. 15 Bifurcation diagrams of the numerical and experimental models at an AoA of 2.5 degrees and flare angles of 10 and 30 degrees. In which the dark and light blues lines represent the maximum and minimum value achieved during an LCO

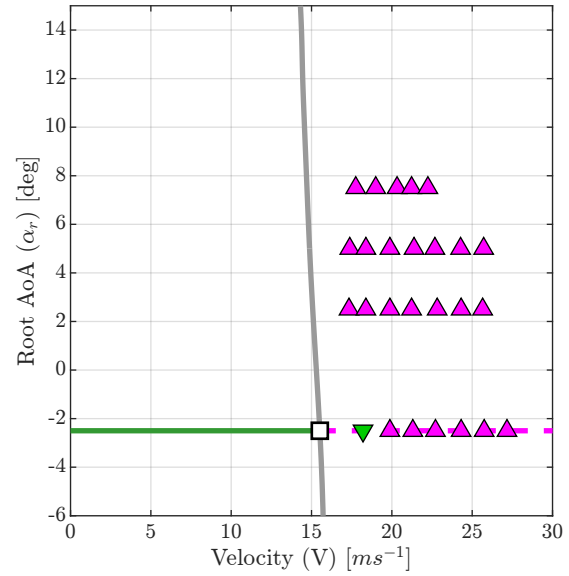


Fig. 16 Bifurcation diagram showing the predicted linear flutter boundary using two parameter continuation at a flare angle of 30 degrees

bifurcation between the two models, as well as a 5 degree difference between the predicted equilibrium fold angles. These discrepancies are assumed to emanate from the approximation made in section III.A in which it was assumed that the structural model folded about a hinge line with zero flare angle. This approximation significantly reduced the complexity of the equations of motion, enabling them to be analytically calculated using the Euler-Lagrange approach, and is likely a good approximation for low flare angles. However, in the case of a 30 degree flare angle, it is likely that the chordwise motion of the wingtip with fold angle could have a large impacts of the dynamics of the system.

Nevertheless, referring back to Fig. 15, the linear flutter boundary of the *flare30* case is significantly less than that of the *flare10* case, which is also predicted by experiment. This difference is due to the increased aerodynamic stiffness of the FFWT at larger flare angles, as shown in Fig. 13, leading to the faster increase in the wingtip flapping frequency, and therefore an earlier coalescence of the first two modes, as shown in Fig. 17.

Additionally, Fig. 13 suggests that the variation in the aerodynamic stiffness with root AoA in the *flare30* case may be significantly less than in the *flare10* case, and therefore should be less variation in the velocity of the linear flutter boundary. Once again, by starting from point A in Fig. 15 and conducting two parameter continuation using the velocity and root AoA as parameters, the linear flutter boundary of the system can be predicted. Figure 16 shows that there is significantly less variation in the linear flutter boundary in the *flare30* case when compared to the *flare10* case, shown in Fig. 14. Unfortunately, it was difficult to measure this boundary experimentally due to the wingtip stalling at lower velocities, significantly changing both the fold angle of the equilibrium position and the dynamics of the system.

Aerodynamic stall can also be an important consideration when evaluating the mechanism which stabilises an LCO. Figure 18 shows how the local AoA at the root, mid-span and tip of the FFWT varied around one cycle of a stable LCO at points: P1 in Fig. 11, and P2 and P3 in Fig. 15. P1 refers to the *flare10* case, and as already indicated in Fig. 10, shows that the magnitude of the local AoA on the wingtip never goes above the stall angle. Therefore this LCO is stabilised by geometric nonlinearities alone. This effect was seen qualitatively in the wind tunnel experiments; as seen in Fig. 19a, at the point of minimum fold angle the flow is attached across the entire wingtip and there was no sign of stall at any point during the oscillations.

P2 and P3 in Figs. 15 and 18, refer to the *flare30* case. At P2, which is close to the Hopf bifurcation, stall is only present at the tip of the wingtip during the down stroke (the wingtip moving from a more positive to a more negative fold angle). The shape of the phase plot in Fig. 15 for P2 is similar to that of P1, suggesting that the geometric nonlinearities are still the primary mechanism stabilising the LCOs at higher flare angles. As the velocity is increased the motion of the wingtip becomes more violent, with greater induced velocities seen across the span of the wingtip, this leads to large

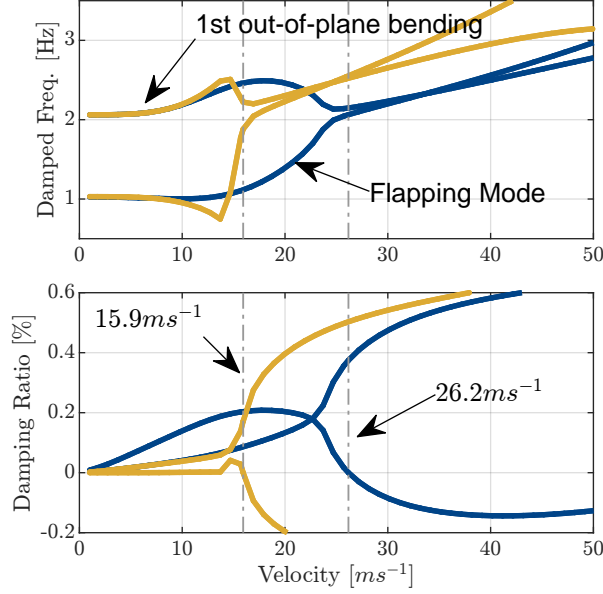


Fig. 17 Variation of damped frequency and damping ratio for the first two modes, at an AoA of 2.5 deg and a flare angle of 10 and 30 deg.

regions of stall, particularly on the down stroke, as seen in both P3 in Fig. 15 and experimentally in Fig. 19b.

Regarding Fig. 15, there are three primary mechanisms defining the local AoA of a FFWT during an LCO. Firstly, the geometric AoA of a FFWT varies with fold angle, appearing as a single curve in Fig. 15 resembling the curves shown in Fig. 13. Secondly, as the FFWT flaps up and down, there is an induced velocity which decreases the local AoA when the wingtip is moving down and increases the local AoA when it is moving up. In the case of a wingtip with a flare angle of zero degrees, this would result in an symmetrical ellipse in its equivalent plot to Fig. 15. Additionally, by moving from a point located at the hinge towards one located at the tip of the wingtip, the induced velocities become larger, increasing the amplitude of the ellipse. Thirdly, the vertical heaving motion at the tip of the inner wing induces a velocity on the wingtip, which is negative when the inner wing moves up and positive when it moves down. The magnitude of this effect on the FFWT is dependent of the fold angle, as at a fold angle of ± 90 degrees, the heaving motion would not change the local AoA of the wingtip.

The paths shown in Fig. 15 are primarily a combination of these three effects. For example, considering P2, the local AoA is biased towards more positive values at negative fold angles, due to the geometric AoA of the FFWT, and the elliptical shape at the tip of the FFWT is due to the induced velocities due to the flapping motion of the FFWT. At P3, the amplitude of the LCO is much larger, hence so are the induced velocities at the tip of the FFWT. Therefore, the curve becomes more elliptical, moving the peak local AoA closer to the mean fold angle when compared to P2.

Another point of interest from Fig. 15 is the local AoA at the root of the wingtip. Noting that in Fig. 15 one cycle moves from lighter colours to darker colours, you can see that the local AoA at the root varies in the opposite way to the tip of wing, with the maximum AoA instead occurring during the upstroke. This phenomenon is driven by the heaving motion of the inner wing and suggests the motion of the inner wing and wingtip are out of phase during the LCO.

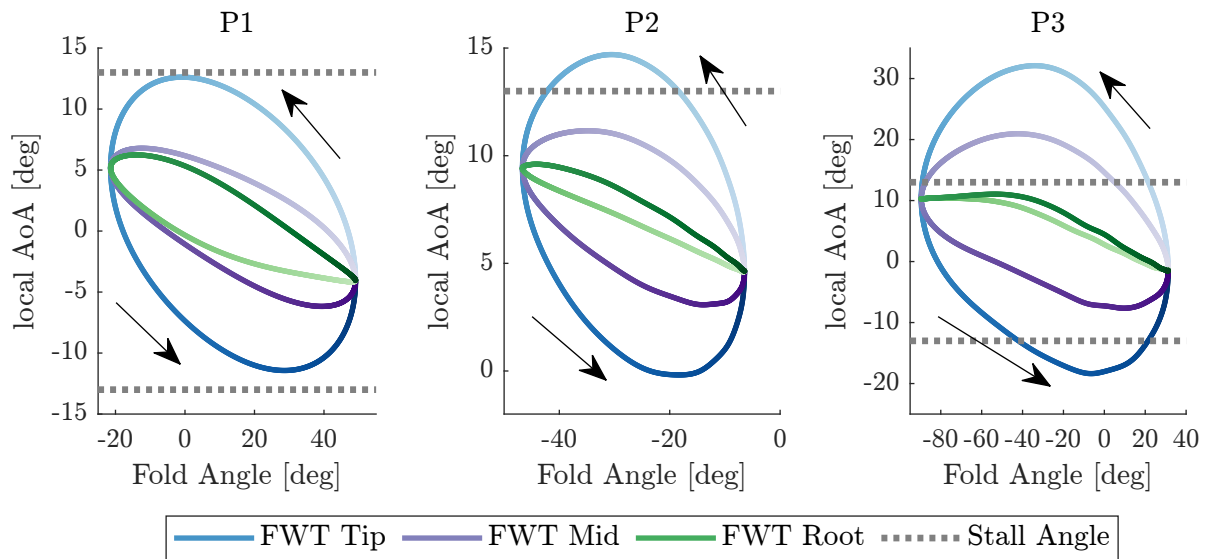


Fig. 18 Phase space plot showing the variation in both the fold angle and local AoA at the root, mid-span, and tip of the FWT at points: P1 in Fig. 11, and P2 and P3 in Fig. 15

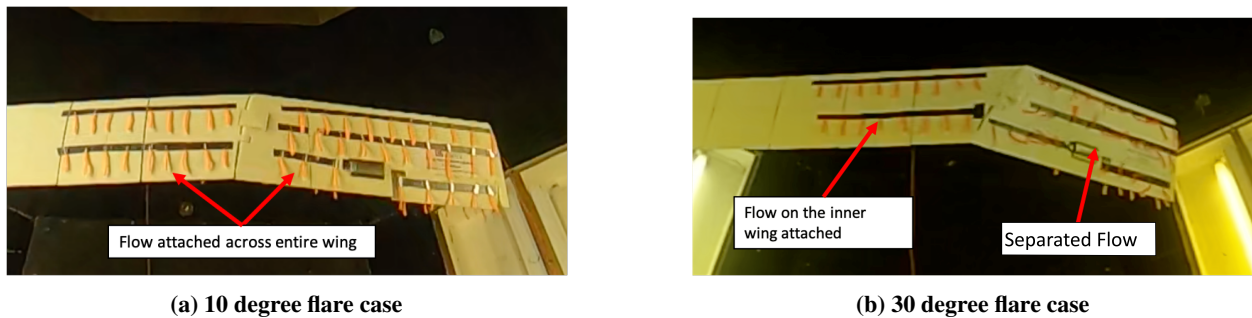


Fig. 19 Images showing the qualitative state of flow attachment at the minimum fold angle of an LCO, for different flare angles

V. Effect of the Wingtip Tab

In the previous section, it was shown that the dynamic behaviour of a wing incorporating an FFWT depends on the root AoA. This effect was assumed to be caused by the equilibrium position of the wingtip varying with root AoA, which changed the aerodynamic stiffness of the wingtip. To confirm this explanation, it is hypothesised that if the equilibrium position of the wingtip could be varied by some other means, such as by the use of a control surface on the wingtip, the aerodynamic stiffness could be varied, altering the dynamic behaviour of the system. As outlined in section II.A and shown in Fig. 2, the FFWT of the wind tunnel model was equipped with such an additional control surface, which was used in a previous study to augmented the gust load alleviation of FFWTs [21].

Figure 20 shows the bifurcation diagrams for the numerical model at an AoA of 2.5 degrees, 10 degrees flare angle, and 3 wingtip tab angles of -10, 0 and 10 degrees. Figure 20 indicates that changing the wingtip tab angle varies both the static equilibrium position of the wingtip as well as the velocity at which the Hopf bifurcation occurs. By conducting two parameter continuation from point A in Fig. 20, using velocity and tab angle as the continuation parameters, a locus of Hopf bifurcations can be constructed describing the linear stability boundary of the system, which is shown in Fig. 21. This figure shows that in both the experimental and numerical results, the use of a wingtip tab can alter the dynamic behaviour of a system incorporating an FFWT, altering the linear flutter speed. Although qualitatively similar, Table 7 indicates that at large tab angles, larger changes are seen in the stability boundary of the numerical model, implying that the efficiency of the tab used in the numerical model is over-predicted at large tab angles, which is unsurprising given the linear nature of the model used to predict the effect of the tab, as described in section III.B.

Nevertheless, an interesting conclusion of Fig. 21 is the suggestion that the stability of the system can be altered 'in flight' by changing the wingtip tab angle. A visualisation of this effect is shown both experimentally and numerically in Fig. 22. In this figure both models are initially started from point B in Fig. 21 (in the case of the experimental model, this was achieved by pulling the cord attached just inboard of the hinge taut, then gently releasing it). From here an instability grows exponentially until it is bounded by some nonlinearity and a stable LCO is formed. After 15 seconds the wingtip tab angle is changed to -15 degrees (point C in Fig. 21), after which the instability quickly decays away in both the experimental and numerical time traces. Figure 22 highlights that an additional control surface on the wingtip could be used to extend the flutter boundary of an aircraft incorporating FFWTs, in addition to reducing peak gust loading [21], and improving the roll control of an aircraft [56]. It should however be noted that due to the increased wingtip aerodynamic stiffness with flare angle, this effect will be most prevalent a low flare angles, at which a tab has

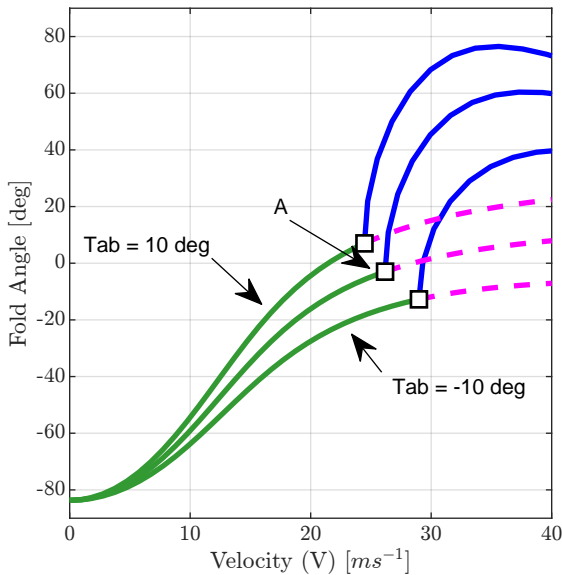


Fig. 20 Bifurcation diagrams of the numerical model, at a root AoA of 2.5 degrees, flare angle of 10 degrees, and 3 wingtip tab angles (-10, 0 and 10 degrees)

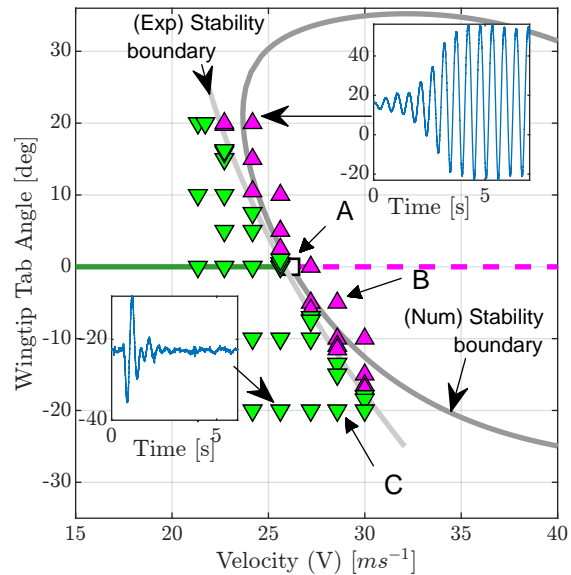


Fig. 21 Bifurcation diagram of the experimental and numerical models at an AoA of 2.5 degrees and a flare angle of 10 degrees. Including corresponding experimental time traces, and the estimated experimental and numerical stability boundaries.

Table 7 Tabulated flutter speeds for a selection of tab angles from Fig. 21. The experimental values use the estimated stability boundary shown in Fig. 21.

Tab Angle [deg]	Experimental [ms^{-1}]	Numerical [ms^{-1}]
20	22.5	23.7
10	24.0	24.4
0	25.8	26.2
-10	28.0	28.9

more authority over the fold angle of the wingtip.

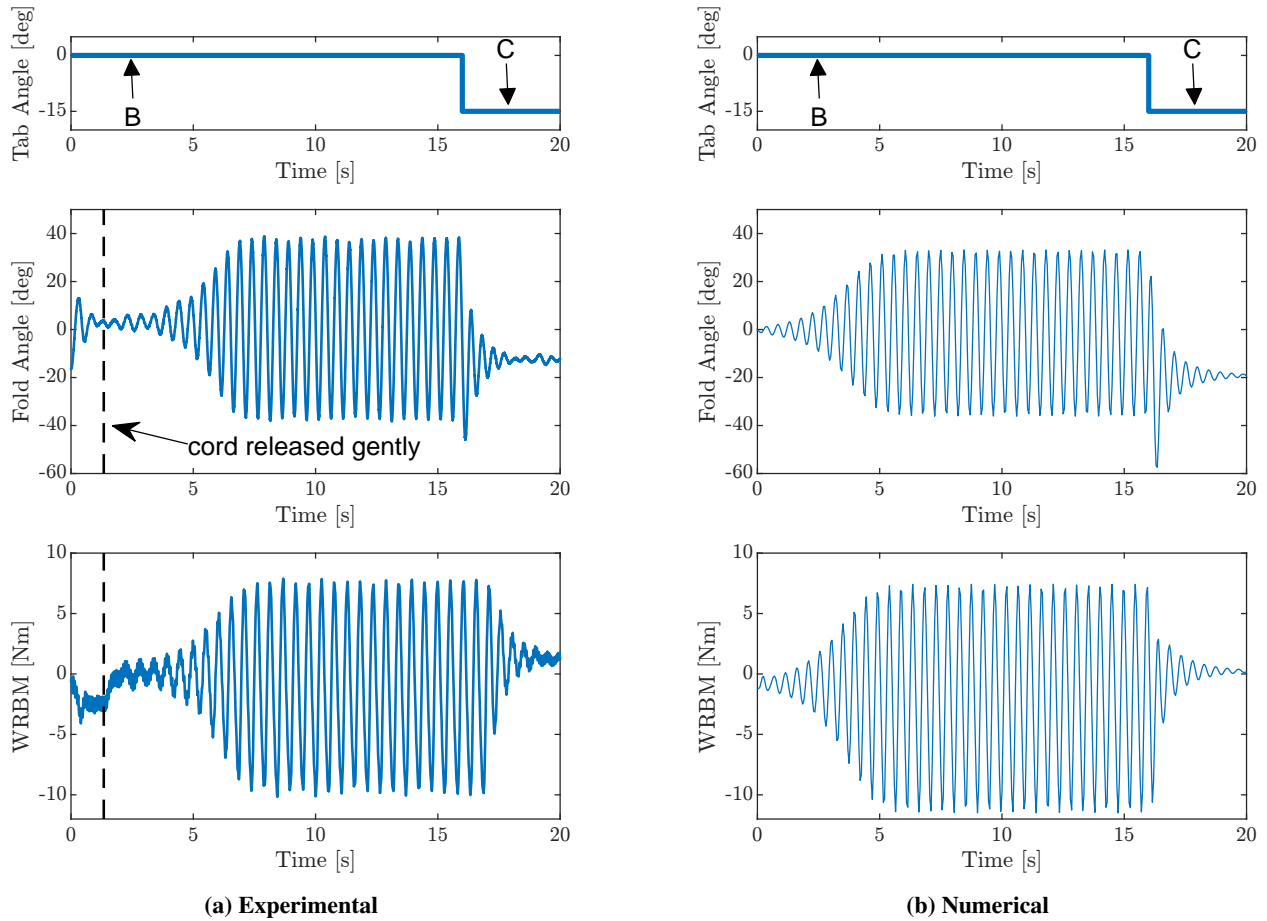


Fig. 22 Experimental and numerical time traces showing the growth of an LCO at an AoA of 2.5 deg and a velocity of 26.8 ms^{-1} , then the LCO being stabilised by changing the tab angle

VI. Conclusions

This paper presents the first experimental research into the nonlinear dynamic behaviour of a wing incorporating flared folding wingtips (FFWTs) at velocities beyond its flutter boundary. These results were also compared to a low fidelity numerical model, which incorporated both a geometrically nonlinear folding wingtip and a simplified aerodynamic stall model, to provide a more complete insight into how the dynamics of an FFWT vary with selected parameters both before and after the linear flutter speed.

The presented results show that beyond the flutter boundary, a stable limit cycle oscillation (LCO) forms. This LCO was shown to be predominately bounded by geometric nonlinearities, as in most conditions the local AoA on the wingtip remained small during the oscillations.

Continuation and bifurcation techniques were also utilised for the first time to give a more complete insight into the nonlinear dynamics of a wing incorporating an FFWT. In particular, bifurcation analysis was used to: identify how the location of the linear flutter boundary varies with both wind speed and root angle of attack, and track the amplitude of the LCO that forms beyond the boundary, with good a correlation observed between these results and the experimental data, particularly at low flare angles.

Also presented is the effect of a wingtip tab on the stability boundary of a wing incorporating FFWTs. Experimental and numerical two-parameter continuation plots were produced to show that the tab angle can significantly alter the stability boundary of the system, indicating that the choice of aerofoil shape is an important parameter when considering the stability boundary of FFWTs, and that a movable control surface on an FFWT could be used 'in-flight' to extend the stability boundary of an aircraft.

Acknowledgments

The first author is supported via an Engineering and Physical Science Research Council (EPSRC) iCASE award (19000004) sponsored by Airbus Operations UK Ltd.

References

- [1] Lee, D. S., Fahey, D. W., Skowron, A., Allen, M. R., Burkhardt, U., Chen, Q., Doherty, S. J., Freeman, S., Forster, P. M., Fuglestedt, J., Gettelman, A., De León, R. R., Lim, L. L., Lund, M. T., Millar, R. J., Owen, B., Penner, J. E., Pitari, G., Prather, M. J., Sausen, R., and Wilcox, L. J., "The Contribution of Global Aviation to Anthropogenic Climate Forcing for 2000 to 2018," *Atmospheric Environment*, Vol. 244, 2021, p. 117834. <https://doi.org/10.1016/j.atmosenv.2020.117834>.
- [2] Fichert, F., Forsyth, P., and Niemeier, H.-M., *Aviation and Climate Change: Economic Perspectives on Greenhouse Gas Reduction Policies*, 1st ed., Routledge, London, 2020. <https://doi.org/10.4324/9781315572406>.
- [3] Bradley, M. K., Dronney, C. K., and Allen, T. J., "Subsonic Ultra Green Aircraft Research. Phase II-Volume I; Truss Braced Wing Design Exploration," Tech. Rep. CR-2015-218704, NASA, 2015. URL <https://ntrs.nasa.gov/citations/20150017036>.
- [4] Drela, M., "Development of the D8 Transport Configuration," 29th AIAA Applied Aerodynamics Conference, Honolulu, Hawaii, 2011. <https://doi.org/10.2514/6.2011-3970>.
- [5] Kroo, I., "Drag Due to Lift: Concepts for Prediction and Reduction," *Annual Review of Fluid Mechanics*, Vol. 33, No. 1, 2001, pp. 587–617. <https://doi.org/10.1146/annurev.fluid.33.1.587>.
- [6] Anon, *Annex 14*, 8th ed., Aerodromes, Vol. 1, International Civil Aviation Organization, Montréal, Quebec, 2018.
- [7] Barnes, C. H., *Shorts Aircraft since 1900*, Putnam; Aero Publishers, London; Fallbrook (Calif.), 1967.
- [8] Lassen, M., Douglas, C., Jones, K. T., and Kenning, T. B., *Wing Fold Controller*, Office, European Patent, 2018. EP2727829B1.
- [9] Barbarino, S., Bilgen, O., Ajaj, R., Friswell, M., and Inman, D., "A Review of Morphing Aircraft," *Journal of Intelligent Material Systems and Structures - J INTEL MAT SYST STRUCT*, Vol. 22, 2011. <https://doi.org/10.1177/1045389X11414084>.
- [10] Bourdin, P., Gatto, A., and Friswell, M. I., "Aircraft Control Via Variable Cant-Angle Winglets," *Journal of Aircraft*, Vol. 45, No. 2, 2008, pp. 414–423. <https://doi.org/10.2514/1.27720>.
- [11] Gatto, A., Bourdin, P., and Friswell, M. I., "Experimental Investigation into the Control and Load Alleviation Capabilities of Articulated Winglets," *International Journal of Aerospace Engineering*, Vol. 2012, 2012, pp. 1–15. <https://doi.org/10.1155/2012/789501>.

- [12] Mills, J., and Ajaj, R., "Flight Dynamics and Control Using Folding Wingtips: An Experimental Study," *Aerospace*, Vol. 4, No. 2, 2017, p. 19. <https://doi.org/10.3390/aerospace4020019>.
- [13] Rogerson, D. B., "Technological Advancements Resulting from Xb-70 Performance Requirements," SAE Technical Paper 650798, 1965. <https://doi.org/10.4271/650798>.
- [14] Guerrero, J., Sanguineti, M., and Wittkowski, K., "Cfd Study of the Impact of Variable Cant Angle Winglets on Total Drag Reduction," *Aerospace*, Vol. 5, No. 4, 2018, p. 126. <https://doi.org/10.3390/aerospace5040126>.
- [15] Daniele, E., De Fenza, A., and Vecchia, P., "Conceptual Adaptive Wing-Tip Design for Pollution Reductions," *Journal of Intelligent Material Systems and Structures - J INTEL MAT SYST STRUCT*, Vol. 23, 2012, pp. 1197–1212. <https://doi.org/10.1177/1045389X12445030>.
- [16] Wang, C., Khodaparast, H., and Friswell, M., "Investigating the Benefits of Morphing Wing Tip Devices - a Case Study," International Forum on Aeroelasticity and Structural Dynamics, Saint Petersburg, Russia, 2015.
- [17] Castrichini, A., Siddaramaiah, V. H., Calderon, D. E., Cooper, J. E., Wilson, T., and Lemmens, Y., "Preliminary Investigation of Use of Flexible Folding Wing Tips for Static and Dynamic Load Alleviation," *The Aeronautical Journal*, Vol. 121, No. 1235, 2017, pp. 73–94. <https://doi.org/10.1017/aer.2016.108>.
- [18] Cheung, R. C. M., Rezgui, D., Cooper, J. E., and Wilson, T., "Testing of a Hinged Wingtip Device for Gust Loads Alleviation," *Journal of Aircraft*, Vol. 55, No. 5, 2018, pp. 2050–2067. <https://doi.org/10.2514/1.c034811>.
- [19] Castrichini, A., Hodigere Siddaramaiah, V., Calderon, D. E., Cooper, J. E., Wilson, T., and Lemmens, Y., "Nonlinear Folding Wing Tips for Gust Loads Alleviation," *Journal of Aircraft*, Vol. 53, No. 5, 2016, pp. 1391–1399. <https://doi.org/10.2514/1.c033474>.
- [20] Castrichini, A., Wilson, T., Saltari, F., Mastroddi, F., Viceconti, N., and Cooper, J., "Aeroelastic Flight Dynamics Coupling Effects of the Semi-Aeroelastic Hinge Device," *Journal of Aircraft*, 2019, pp. 1–9. <https://doi.org/10.2514/1.C035602>.
- [21] Cheung, R. C. M., Rezgui, D., Cooper, J. E., and Wilson, T., "Testing of Folding Wingtip for Gust Load Alleviation of Flexible High-Aspect-Ratio Wing," *Journal of Aircraft*, 2020, pp. 1–13. <https://doi.org/10.2514/1.c035732>.
- [22] Eguea, J. P., Pereira Gouveia Da Silva, G., and Martini Catalano, F., "Fuel Efficiency Improvement on a Business Jet Using a Camber Morphing Winglet Concept," *Aerospace Science and Technology*, Vol. 96, 2020. <https://doi.org/10.1016/j.ast.2019.105542>.
- [23] Dussart, G., Yusuf, S., and Lone, M., "Identification of in-Flight Wingtip Folding Effects on the Roll Characteristics of a Flexible Aircraft," *Aerospace*, Vol. 6, No. 6, 2019, p. 63. <https://doi.org/10.3390/aerospace6060063>.
- [24] Balatti, D., Haddad Khodaparast, H., Friswell, M. I., Manolesos, M., and Amoozgar, M., "The Effect of Folding Wingtips on the Worst-Case Gust Loads of a Simplified Aircraft Model," *Proceedings of the Institution of Mechanical Engineers, Part G: Journal of Aerospace Engineering*, 2021. <https://doi.org/10.1177/09544100211010915>.
- [25] Healy, F., Cheung, R., Neofet, T., Lowenberg, M., Rezgui, D., Cooper, J., Castrichini, A., and Wilson, T., "Folding Wingtips for Improved Roll Performance," *Journal of Aircraft*, 2021, pp. 1–14. <https://doi.org/10.2514/1.C036372>.
- [26] Rouanet, R. L. M. F., and Res, F. V., *Aircraft*, Office, Us Patent, 1938. US2186558A.
- [27] Anon, "Wind Tunnel Tests and Further Analysis of the Floating Wing Fuel Tanks for Helicopter Range Extension. Volume 1: Helicopter Range Extension Wind Tunnel Study," Tech. rep., Boeing Airplane Company, 1960.
- [28] Lockett, B., *Flying Aircraft Carriers of the Usaf: Wing Tip Coupling*, 1st ed., LockettBooks, 2009.
- [29] Howcroft, C., Calderon, D., Lambert, L., Castellani, M., Cooper, J. E., Lowenberg, M. H., and Neild, S., "Aeroelastic Modelling of Highly Flexible Wings," 15th Dynamics Specialists Conference, San Diego, California, USA, 2016. <https://doi.org/10.2514/6.2016-1798>.
- [30] Healy, F., Cheung, R., Rezgui, D., Cooper, J., Wilson, T., and Castrichini, A., "On the Effect of Geometric Nonlinearity on the Dynamics of Flared Folding Wingtips," *Journal of Aircraft*, 2022, pp. 1–14. <https://doi.org/10.2514/1.C036877>.
- [31] Dowell, E., Edwards, J., and Strganac, T., "Nonlinear Aeroelasticity," *Journal of Aircraft*, Vol. 40, No. 5, 2003, pp. 857–874. <https://doi.org/10.2514/2.6876>.
- [32] Wilson, T., Castrichini, A., Paterson, J., and Arribas Ardura, R., "Non-Linear Aeroelastic Behaviour of Hinged Wing Tips," 6th Aircraft Structural Design Conference, We The Curious, Bristol, UK, 2018. <https://doi.org/10.2514/6.2017-0502>.

- [33] Mastracci, P., Saltari, F., Mastroddi, F., Wilson, T., and Castrichini, A., “Unsteady Aeroelastic Analysis of the Semi Aeroelastic Hinge Including Local Geometric Nonlinearities,” *AIAA Journal*, Vol. 60, No. 5, 2022, pp. 3147–3165. <https://doi.org/10.2514/1.J061108>.
- [34] Sharma, S., Coetzee, E. B., Lowenberg, M. H., Neild, S. A., and Krauskopf, B., “Numerical Continuation and Bifurcation Analysis in Aircraft Design: An Industrial Perspective,” *Philos Trans A Math Phys Eng Sci*, Vol. 373, No. 2051, 2015. <https://doi.org/10.1098/rsta.2014.0406>.
- [35] Eaton, A., Howcroft, C., Coetzee, E., Neild, S., Lowenberg, M., and Cooper, J., “Numerical Continuation of Limit Cycle Oscillations and Bifurcations in High-Aspect-Ratio Wings,” *Aerospace*, Vol. 5, No. 3, 2018. <https://doi.org/10.3390/aerospace5030078>.
- [36] Mair, C., Rezgui, D., and Titurus, B., “Nonlinear Stability Analysis of Whirl Flutter in a Rotor-Nacelle System,” *Nonlinear Dyn*, Vol. 94, No. 3, 2018, pp. 2013–2032. <https://doi.org/10.1007/s11071-018-4472-y>.
- [37] Alighanbari, H., and Price, S. J., “The Post-Hopf-Bifurcation Response of an Airfoil in Incompressible Two-Dimensional Flow,” *Nonlinear Dynamics*, Vol. 10, No. 4, 1996, pp. 381–400. <https://doi.org/10.1007/BF00045483>.
- [38] Gee, D. J., “Numerical Continuation Applied to Panel Flutter,” *Nonlinear Dynamics*, Vol. 22, No. 3, 2000, pp. 271–280. <https://doi.org/10.1023/A:1008374401581>.
- [39] Dimitriadis, G., “Bifurcation Analysis of Aircraft with Structural Nonlinearity and Freeplay Using Numerical Continuation,” *Journal of Aircraft*, Vol. 45, No. 3, 2008. <https://doi.org/10.2514/1.28759>.
- [40] Cheung, R. C., Rezgui, D., Cooper, J. E., and Wilson, T., “Analyzing the Dynamic Behavior of a High Aspect Ratio Wing Incorporating a Folding Wingtip,” AIAA Scitech 2020 Forum, Orlando, Florida, 2020. <https://doi.org/10.2514/6.2020-2290>.
- [41] *Matlab R2020b*, Software Package, Ver. 9.9.0.1592791, The MathWorks Inc., Natick, Massachusetts, 2020.
- [42] Arda Ozdemir, A., and Gumussoy, S., “Transfer Function Estimation in System Identification Toolbox Via Vector Fitting,” *IFAC-PapersOnLine*, Vol. 50, No. 1, 2017, pp. 6232–6237. <https://doi.org/https://doi.org/10.1016/j.ifacol.2017.08.1026>.
- [43] Wright, J., and Cooper, J. E., *Introduction to Aircraft Aeroelasticity and Loads*, Aerospace Series, Wiley, Chichester UK, 2015. <https://doi.org/10.1002/9781118700440>.
- [44] Murray, R. M., *A Mathematical Introduction to Robotic Manipulation*, 1st ed., Routledge, Boca Raton, 1994.
- [45] Meurer, A., Smith, C. P., Paprocki, M., Certik, O., Kirpichev, S. B., Rocklin, M., Kumar, A., Ivanov, S., Moore, J. K., Singh, S., Rathnayake, T., Vig, S., Granger, B. E., Muller, R. P., Bonazzi, F., Gupta, H., Vats, S., Johansson, F., Pedregosa, F., Curry, M. J., Terrel, A. R., Roucka, S., Saboo, A., Fernando, I., Kulal, S., Cimrman, R., and Scopatz, A., “SymPy: Symbolic Computing in Python,” *PeerJ Computer Science*, Vol. 3, 2017, p. e103. <https://doi.org/10.7717/peerj-cs.103>.
- [46] Sharpe, P. D., “Aerosandbox: A Differentiable Framework for Aircraft Design Optimization,” Ph.D. thesis, Massachusetts Institute of Technology, 2021. URL <https://hdl.handle.net/1721.1/131194>.
- [47] Drela, M., “Xfoil: An Analysis and Design System for Low Reynolds Number Airfoils,” *Low Reynolds Number Aerodynamics*, edited by T. J. Mueller, Springer Berlin Heidelberg, 1989, pp. 1–12. https://doi.org/10.1007/978-3-642-84010-4_1.
- [48] Klimek, M., and Perelstein, M., “Neural Network-Based Approach to Phase Space Integration,” *SciPost Physics*, Vol. 9, No. 4, 2020. <https://doi.org/10.21468/SciPostPhys.9.4.053>.
- [49] Delaurier, J., “An Aerodynamic Model for Flapping-Wing Flight,” *The Aeronautical Journal*, Vol. 97, No. 964, 1993, pp. 125–130. <https://doi.org/10.1017/S0001924000026002>.
- [50] Scherer, J., “Experimental and Theoretical Investigation of Large Amplitude Oscillation Foil Propulsion Systems,” Tech. Rep. TR-662-1-F, Hydonautics Inc., 1968.
- [51] Kuznetsov, Y., *Elements of Applied Bifurcation Theory*, 3rd ed., Applied Mathematical Sciences, Springer-Verlag New York, 2004. <https://doi.org/10.1007/978-1-4757-3978-7>.
- [52] Kuchment, P., *Floquet Theory for Partial Differential Equations*, 1st ed., Operator Theory: Advances and Applications, Birkhäuser Basel, 1993. <https://doi.org/10.1007/978-3-0348-8573-7>.
- [53] Coetzee, E. B., Krauskopf, B., and Lowenberg, M. H., “The Dynamical Systems Toolbox: Integrating Auto into Matlab,” 16th US National Congress on Theoretical and Applied Mechanics, State College, Pennsylvania, 2010.

- [54] Doedel, E. J., Fairgrieve, T. F., Sandstede, B., Champneys, A. R., Kuznetsov, Y. A., and Wang, X., “Auto-07p: Continuation and Bifurcation Software for Ordinary Differential Equations,” Tech. rep., 2007.
- [55] Dimitriadis, G., *Introduction to Nonlinear Aeroelasticity*, John Wiley and Sons Ltd, 2017, chap. 2, pp. 9–61. <https://doi.org/10.1002/9781118756478.ch2>.
- [56] Blunt, W., Healy, F., Cheung, R., Lowenberg, M., and Cooper, J., “Trailing Edge Tabs on Folding Wingtips (Fwts) for Aircraft Roll Control,” AIAA Scitech Forum 2022, San Deigo, United States, 2022. <https://doi.org/10.2514/6.2022-0692>.